Beyond the Born-Oppenheimer static surface model for molecule-surface reactions

Spiering, P.

Chapter 3

An Improved Static Corrugation Model

This chapter is based on P. Spiering, M. Wijzenbroek, and M. F. Somers. "An Improved Static Corrugation Model". In: *J. Chem. Phys.* 149 (2018), p. 234702.

Abstract

Accurately describing surface temperature effects for the dissociation of H_2 on Cu(111) remains challenging. While Ab initio Molecular Dynamics (AIMD), the current state-of-the-art method for modelling such systems, can produce accurate results, it is computationally too expensive to use for extensive testing of, for example, density functionals. A chemically accurate static corrugation model for H_2 and D_2 on Cu(111) dissociation was made by introducing effective three-body interactions as well as an H_2-bond dependence and fitting the model to density functional theory energies for 15113 different configurations. Reaction probabilities and rovibrational (in)elastic scattering probabilities were computed and compared to experiments and other calculations. Theoretical and experimental results are in good agreement, except for the reaction of (v=0, J=0) H_2 where both AIMD and the newly developed static corrugation model, both based on the same underlying density functional, predict a similar deviation from experiment.

3.1 Introduction

Heterogeneously catalysed processes such as the Haber-Bosch [2] process and the hydrogen and oxygen evolution reactions of water splitting [3] are essential for modern day industry. To gain insight into how these processes are catalysed efficiently, for example by metal interfaces, the reaction mechanism is broken down into elementary reaction steps, which are subsequently studied individually. Understanding these elementary reaction steps can then, hopefully, lead to better catalysis of chemical processes on surfaces. One such elementary reaction step is the dissociation of H_2 and D_2 on Cu(111), which has been extensively studied both experimentally [4–9] and theoretically [10–17].

For modeling such systems, the Born-Oppenheimer approximation (BOA) is often used to separate the nuclear and electron dynamics. A ground state electronic structure theory such as density functional theory (DFT) is then used to compute the energy at several nuclear configurations resulting in a potential energy surface (PES). For the dissociative chemisorption probabilities of H_2 and D_2 on Cu(111), it is known that the BOA performs well [18, 19] and the small effect that is present is discussed extensively

in Chap. 4. One way to determine the overall accuracy of the electronic structure is to calculate the probability of H_2 reacting on the Cu(111) surface at specific translational and rovibrational energies and compare the result with experiments. DFT can be used together with the specific reaction parameter (SRP) method to compute a chemically accurate PES for the H_2 on Cu(111) system [12].

In practice, chemical processes at surfaces are performed at high surface temperatures, which complicates the fundamental understanding even further. To include the effect of surface temperature on the dissociation of H_2 and D_2 on Cu(111) however, the PES must somehow take surface displacements into account. It is computationally convenient to reduce the PES to a 6D PES [15, 16] and describe the effect of surface displacements as a perturbation of the 6D PES. This was done previously with the static corrugation model (SCM) [14]. Here it was assumed that H_2 interacts with essentially a static snapshot of a thermally equilibrated Cu(111) surface. This was motivated for H_2 and D_2 on Cu(111) due to the large mass mismatch allowing no significant energy exchange due to collisions of the molecule with the surface. Furthermore, the comparatively slow velocity of thermally equilibrated Cu atoms results in no significant surface motion during the short interaction time of H_2 at the Cu(111) surface. In contrast, it is also possible to compute the electronic structure on an "as needed" basis using ab-initio molecular dynamics (AIMD) [10], circumventing the need to make any further approximations, albeit at increased computational effort. The SCM was able to reproduce experimental and AIMD molecular beam experiments [10] within chemical accuracy (1 kcal/mol), even though the results of the fitting procedure used suggested that the errors should be larger. Recently it has also become possible to use high-dimensional neural network potentials [20–22] (HD-NNP) to describe the effect of surface displacements in molecule surface reactions. This method has also been used in Chap. 5. While this seems a promising alternative to both AIMD and the SCM, I am not aware of any accurate HD-NNP for H_2 on Cu(111), using the same DFT functional as was used for AIMD [10], at the moment of writing.

Our goal is now to improve the SCM for the H_2 and D_2 on Cu(111) system to even more accurately reproduce the results of AIMD and experimental data, while

maintaining the advantage in computational effort.

3.2 Methods

3.2.1 Ab Initio Calculations for H_2 at Cu(111)

For the H_2 on Cu(111) system a chemically accurate SRP functional [11, 12] has been created by taking a linear combination of 0.52 PBE [23] and 0.48 RPBE [24]. To be able to compare the SCM to previous AIMD results, the underlying PES should be reproduced as closely as possible. This was done by performing ground state DFT calculations using the Vienna Ab-initio Simulation Package (VASP) [25–27]. Calculations were performed using the Ultra-Soft (US) pseudopotentials [25, 27] provided by VASP, an 8 by 8 by 1 Γ-centered k-point grid, an energy cut-off of 350 eV for the planewave basis set, a Fermi-smearing with a temperature corresponding to 0.1 eV and a convergence criterion of 0.1 meV.

Figure 3.1 shows a schematic overview of the H_2 on Cu(111) system. The Cu(111) slab has a FCC bulk structure with a cut in the $\langle 111 \rangle$ direction and consists of four layers. These layers are defined using the lattice vectors u and v with u being in the same direction as x while v has an angle of $\frac{\pi}{3}$ with u. The different layers are shifted in u and v of one third of both lattice vectors and the interlayer distances are optimised for a 1 by 1 unit cell. A 3 by 3 unit cell was used in all calculations performed for computing coupling potentials.

3.2.2 Static Corrugation Model

The Static Corrugation Model (SCM) [14] is used to describe the effect of surface temperature due to surface atom displacements on the potential energy surface (PES) of a surface($\overrightarrow{q}$)-adsorbate($\overrightarrow{r}$) system. This is realised by dividing the DFT PES $V_{DFT}(\overrightarrow{q}, \overrightarrow{r})$ into three terms: $V_{DFT}(\overrightarrow{q}^{id}, \overrightarrow{r})$ associated with an ideal surface , V_{strain} associated with distorting a clean surface and V_{coup} associated with the change in the interaction of an adsorbate with the surface due to a surface atom displacement, as

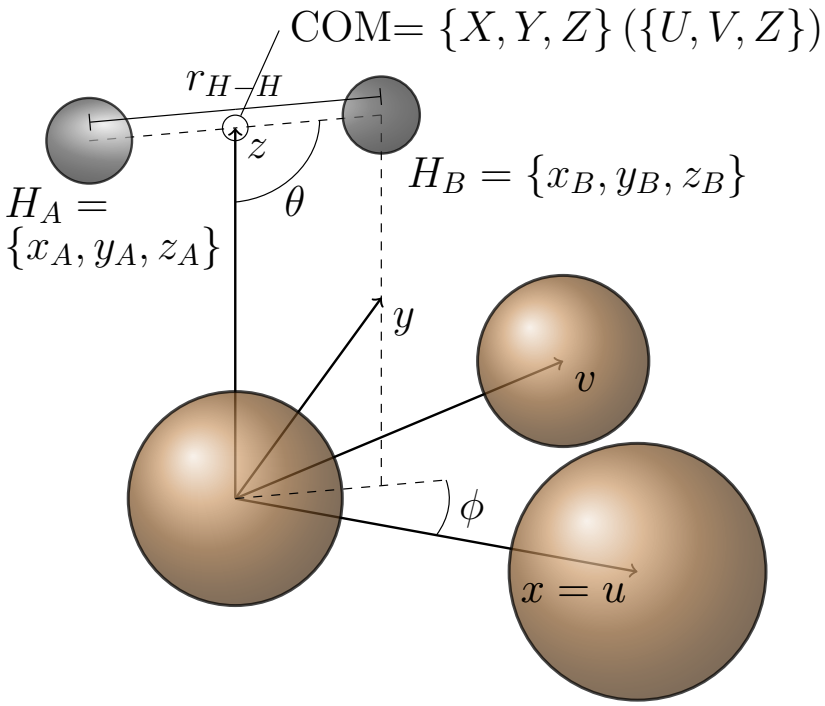

Figure 3.1: Molecular coordinate system of H_2 as well as lattice vectors for Cu(111) are shown. The first layer Cu atoms are indicated in brown while the H atoms are indicated in gray. Indicated are the z, y, $x(= u)$ and v unit vectors. H_2 is described in both an atomic coordinate system, using the position of H_A and H_B on the x, y and z axis as well as a molecular coordinate system using the position X, Y, Z (U, V, Z) of the COM on the x, y and z $(u, v$ and $z)$ axis respectively, together with bond distance r_{H-H}, polar angle θ and azimuthal angle ϕ.

given by

$$V_{DFT}(\overrightarrow{q}, \overrightarrow{r}) = V_{DFT}(\overrightarrow{q}^{id}, \overrightarrow{r}) + V_{coup}(\overrightarrow{r}, \overrightarrow{q}^{id} \rightarrow \overrightarrow{q}) + V_{strain}(\overrightarrow{q}^{id} \rightarrow \overrightarrow{q}), \tag{3.1}$$

where $\overrightarrow{q}$ describes the Cartesian positions of all surface atoms, $\overrightarrow{q}^{id}$ describes the ideal lattice positions in the same way and $\overrightarrow{r}$ describes the Cartesian positions of

all adsorbate atoms (in this chapter only atom A and B). The strain potential $V_{strain}(\overrightarrow{q}^{id} \rightarrow \overrightarrow{q})$ can be neglected for dynamics on a static surface because it is a constant if the surface configuration does not change during the dynamics. Using equation 3.1 and neglecting V_{strain}, the SCM thus approximates the full dimensional DFT PES according to

$$V_{DFT}(\overrightarrow{q}, \overrightarrow{r}) \approx V_{SCM}(\overrightarrow{r}, \overrightarrow{q}^{id} \rightarrow \overrightarrow{q}) = V_{DFT}(\overrightarrow{q}^{id}, \overrightarrow{r}) + V_{coup}(\overrightarrow{r}, \overrightarrow{q}^{id} \rightarrow \overrightarrow{q}). \tag{3.2}$$

To be able to perform dynamics with the static corrugation potential, a continuous representation needs to be found for the ideal lattice $V_{DFT}(\overrightarrow{q}^{id}, \overrightarrow{r})$ as well as the coupling potential $V_{coup}(\overrightarrow{r}, \overrightarrow{q}^{id} \rightarrow \overrightarrow{q})$. It should be noted that HD-NNP could be a good alternative to obtain a continuous representation of the coupling potential $V_{coup}(\overrightarrow{r}, \overrightarrow{q}^{id} \rightarrow \overrightarrow{q})$. However, the work presented in this chapter will continue along the lines of earlier work [14] to be able to make a more thorough comparison. A representation of the SCM potential can be found by interpolating the DFT energies for the ideal surface using the CRP method [15] and fitting the coupling potential with a functional form according to

$$V_{coup}(\overrightarrow{r}, \overrightarrow{q}^{id} \rightarrow \overrightarrow{q}) = \sum_{i}^{\overrightarrow{r}} \sum_{j}^{\overrightarrow{q}} \left(V_{H-Cu}(|\overrightarrow{r}_i - \overrightarrow{q}_j|) - V_{H-Cu}(|\overrightarrow{r}_i - \overrightarrow{q}_j^{id}|) \right), \tag{3.3}$$

where $\overrightarrow{r}_i$ is the Cartesian position of adsorbate atom i, $\overrightarrow{q}_j$ is the Cartesian position of surface atom j and

$$V_{H-Cu}(r) = V_{Ryd} = (1 - \rho(r))V(r) + \rho(r)V(P_7), \tag{3.4}$$

while

$$V(r) = -e^{-P_4(r-P_5)} \cdot \left(\sum_{k=0}^{3} P_k (r - P_5)^k \right), \tag{3.5}$$

and

$$\rho(r) = \begin{cases} 0 & \text{if } r < P_6 \\ \frac{1}{2}\cos\left(\frac{\pi(r-P_7)}{P_7-P_6}\right) + \frac{1}{2} & \text{if } P_6 \leq r \leq P_7 \\ 1 & \text{if } r > P_7 \end{cases}, \tag{3.6}$$

where P_i are the fitted parameters.

The SCM for H_2 on Cu(111) from previous work [14] is extended by including an effective three-body interaction, a corrected surface stretching procedure and a fitting procedure of the coupling potential including many more relevant surface and molecule configurations. We have recalculated the reaction probabilities for the model of Ref. [14] but using an improved implementation of the force scaling due to thermal expansion of the Cu crystal via the stretching procedure.

To include surface expansion due to surface temperature, the CRP potential of the system is stretched by contracting the H_2 COM vectors along the lattice vectors, instead of the Cartesian vectors of the atoms as was done previously. In this way there are no additional small but unwanted contributions to the vibrational and rotational motion due to the stretching procedure. Hence, the full SCM potential becomes

$$V_{SCM}(\vec{r}, \vec{q}, \vec{q}^{id}) = V_{CRP}(\vec{r}^{id}(\vec{r}), \vec{q}^{id}) + \sum_i^{\vec{r}} \sum_j^{\vec{q}} \left(V_{H-Cu}(|\vec{r}_i - \vec{q}_j|) - V_{H-Cu}(|\vec{r}_i^{id}(\vec{r}) - \vec{q}_j^{id}|)\right), \tag{3.7}$$

where $\vec{r}^{id}(\vec{r})$ scales the expanded surface H_2 coordinates $\vec{r}$ along the COM U and V coordinates to the ideal surface in such a way that they correspond to the same relative coordinates. The reaction probabilities using the original SCM model [14] that are reported here using the improved implementation show no major differences compared to the previous results. The above methodology can be used for any 6D PES and is not limited to a CRP PES.

In order to improve upon the SCM, a H-Cu interaction is defined that is not only dependent on the distance between the H_i atom and Cu_j atom (r_{ij}) but also on the H-H bond distance (r_{H-H}). This essentially describes the different behaviour of the H-Cu interaction for H as a part of an H_2 molecule (small r_{H-H}) and for H as an

atom (large r_{H-H}). This was done by making all the parameters P_i of the previous two-body SCM linearly dependent on r_{H-H} as given by

$$P_i = \begin{cases} P_{i,a} r_{H-H}^{min} + P_{i,b} & \text{if } r_{H-H} < r_{H-H}^{min} \\ P_{i,a} r_{H-H} + P_{i,b} & \text{if } r_{H-H}^{min} \leq r_{H-H} \leq r_{H-H}^{max} \\ P_{i,a} r_{H-H}^{max} + P_{i,b} & \text{if } r_{H-H} > r_{H-H}^{max} \end{cases}, \tag{3.8}$$

where r_{H-H}^{min} and r_{H-H}^{max} are cut-off values of the linear dependence set at the smallest and largest value of r_{H-H} used in the fitting procedure. The resulting Rydberg function is then considered an H_2-bond adapted Rydberg function.

3.2.3 Quasi-Classical Dynamics of H_2 and D_2 on Cu(111)

Using either the CRP (V_{CRP}) or SCM PES (V_{SCM}), it is possible to describe the dissociation of H_2 or D_2 on an ideal or non-ideal (with displaced Cu atoms) Cu(111) surface. The PES itself is not a directly measurable observable, so instead molecular beam simulations have been performed. These simulations were performed using the Quasi-Classical (QC) Dynamics [12, 16] method. Initial conditions are determined by using a Monte-Carlo sampling scheme, where zero point energies for the H_2 bond were taken into account only for the initial configurations. Then the system is propagated classically and the resulting trajectory is finally analyzed. We performed 20000 trajectories for each choice of incidence energy E_i, vibrational state v and rotational state J.

The initial conditions for the molecule are generated by first calculating the rovibrational energy levels of the H_2 or D_2 molecule for the used PES using the Fourier grid Hamiltonian method [28]. To get the QC distribution for the H-H bond distance r_{H-H} of the H_2 molecule, the gasphase H_2 molecule was propagated, and positions and momenta were recorded, for one complete phase in its vibration using a constant time step. The initial atomic positions and velocities were then chosen using standard Monte-Carlo methods. The ϕ and θ angles are chosen from an uniform random distribution in the range $[0, 2\pi]$ and $[0, \pi]$ respectively. Angular velocities are chosen according to the quantized angular momentum $L^2 = J(J+1)\hbar^2$ with the angle θ_L

between the angular momentum vector and the surface normal chosen randomly but constrained by $\theta_L = \pi$ if J=0 and $cos(\theta_L) = \frac{m_J}{\sqrt{J(J+1)}}$ if J≥1. The Z component of the COM velocity is set to correspond to a kinetic energy of E_i. The initial COM position is then shifted 9 Å in Z away from the surface (Z=9 Å) while the COM position along the FCC(111) surface is given by $X = \widetilde{U} + \frac{1}{2}\widetilde{V}$ and $Y = \frac{1}{2}\sqrt{3}\widetilde{V}$ where $\widetilde{U}$ and $\widetilde{V}$ are chosen from an uniform random distribution in the range $[0, a]$ with a being the lattice constant. This process was identical to earlier work [10, 12, 14, 16, 17].

The SCM uses the surface atom positions of both the ideal lattice and the corrugated lattice. The ideal lattice is constructed in the same way as the DFT slab used for constructing the CRP with the exception that no periodic boundary conditions are used. Instead, for each trajectory, the initial COM position is projected onto the surface plane and only copper atoms that are from the first three layers and within a radius of 12 Å around the projected COM are considered. The corrugated lattice is constructed from this ideal lattice in three steps. First, the surface expansion along the u and v lattice vectors is introduced. The relative experimentally [29] observed expansion is applied to the lattice constant from the CRP potential. Secondly the interlayer spacings are adjusted in a similar fashion: the experimentally observed relative expansion or contraction [30] in the interlayer spacings is applied to the interlayer spacings used in the DFT slab of the respective CRP potential. Finally, for each surface atom a random direction is chosen and the magnitude of the displacement is randomly selected from an appropriate surface temperature dependent gaussian distribution based on Debye-Waller factors [31].

Once the initial conditions are defined, only the molecule is propagated according to Hamilton's equations of motion with the following hamiltonian (in atomic units):

$$H = \frac{p_A^2(t)}{2m_A} + \frac{p_B^2(t)}{2m_B} + V(R(t)). \tag{3.9}$$

where $p_A(t)$ and $p_B(t)$ are the momenta of atoms A and B respectively at time t and $V(R(t))$ is the potential energy at the Cartesian position $R(t)$ of both atom A and B. The propagation is performed using the predictor-corrector method of Bulirsch and Stoer [32]. A trajectory is considered to be reactive when the H atoms are separated

by more than 2.25 Å before the time cut-off of 20 ps and considered non-reactive otherwise. When a trajectory is non-reactive, the molecule is either trapped as a molecule on the surface, or has scattered to the same or a different rovibrational state which is called elastic or inelastic scattering respectively. No significant contribution of trapped molecules was found during this study and are therefore not reported. The final rovibrational state is determined by binning first to the rotational state based on angular momentum and then to the closest vibrational state in energy with the previously determined rotational state. Results have been obtained for the H_2 and D_2 on Cu(111) system with both an ideal lattice, and a displaced and expanded lattice at a finite surface temperature of T_s=925K.

3.3 Results and Discussion

3.3.1 Coupling potential

To be able to verify and improve the fit of the coupling potentials used in previous work [14] the computation of the coupling potentials is‘ repeated, but this time with the same DFT setup as was used for AIMD calculations [10]. A comparison with these AIMD results and the SCM results can show the importance of surface motion compared to surface displacement. To improve the old SCM model, the new SCM model is fitted to the coupling potential for 15113 configurations instead of 153.

To test the previous assumption that the coupling potential can be approximated with only two-body interactions i.e. H-Cu interactions, the coupling potential are computed at configurations ($\overrightarrow{q}_{id} \rightarrow \overrightarrow{q}_{id} + \overrightarrow{Q}_1 + \overrightarrow{Q}_2$) where two displacements ($\overrightarrow{Q}_1$ and $\overrightarrow{Q}_2$) were made to isolate H-Cu-Cu effective three-body interactions. To compute the H-H-Cu effective three-body interactions, the configurations with the displacements $\overrightarrow{q}_{id} \rightarrow \overrightarrow{q}_{id} + \overrightarrow{Q}$ and $\overrightarrow{r} \rightarrow \overrightarrow{r}'$ were used. This has two advantages, namely fitting these coupling potentials will result in an effective three-body interaction but at the same time it allows us to test how well the two-body approximation performs.

Coupling potentials presented here are computed exactly from DFT calculations

according to

$$V_{coup}(\overrightarrow{r}, \overrightarrow{q}_{id} \rightarrow \overrightarrow{q}_{id} + \overrightarrow{Q}) = V_{DFT}(\overrightarrow{r}, \overrightarrow{q}_{id} + \overrightarrow{Q}) \\ -V_{DFT}(\overrightarrow{r}, \overrightarrow{q}_{id}) - V_{strain}(\overrightarrow{q}_{id} \rightarrow \overrightarrow{q}_{id} + \overrightarrow{Q}), \tag{3.10}$$

where

$$V_{strain}(\overrightarrow{q}_{id} \rightarrow \overrightarrow{q}_{id} + \overrightarrow{Q}) = \\ V_{DFT}(\overrightarrow{r}_{gas}, \overrightarrow{q}_{id} + \overrightarrow{Q}) - V_{DFT}(\overrightarrow{r}_{gas}, \overrightarrow{q}_{id}), \tag{3.11}$$

with $\overrightarrow{r}_{gas}$ indicating that the H_2 molecule has been moved 6 Å away from the surface such that there is essentially no interaction between H_2 and the surface. Here the displacement $\overrightarrow{r} \rightarrow \overrightarrow{r}'$ is understood as simply evaluating the coupling potential at $\overrightarrow{r}'$ instead of $\overrightarrow{r}$.

First the H-Cu-Cu three-body coupling potential is considered. For these coupling potentials, the H_2 was placed at the barrier position of either the bridge, top or HCP site. Two atoms were selected from the first two layers in the surface considering all permutations and symmetries. These were then either moved in all possible combinations of the directions $x(= u)$, y, v and z, as well as both atoms moving towards and away from the H_2 COM. The displacements have a magnitude from -0.3 Å until 0.3 Å with a step of 0.1 Å. There are too many permutations to discuss all of them but a representative selection is discussed next.

Figure 3.2 shows the coupling potentials of the surface displacements of the two surface atoms closest to the H_2 COM perpendicular to the surface and H_2 at the lowest barrier for this system(bridge site barrier). The displacements $\overrightarrow{Q}_1$ and $\overrightarrow{Q}_2$ are in this case symmetric due to the mirror plane along the H bond, meaning that the values for the displacements can be swapped without changing the coupling potential. What is interesting to note here is that the lowest coupling potential is not at the ideal lattice positions (with the displacements at 0 Å) but with the surface atoms slightly moved out of the surface, indicating a puckering [33] effect. This puckering effect can not be taken into account using the SCM (where static surface configurations are Monte-Carlo sampled randomly), however it is not expected to have a large influence

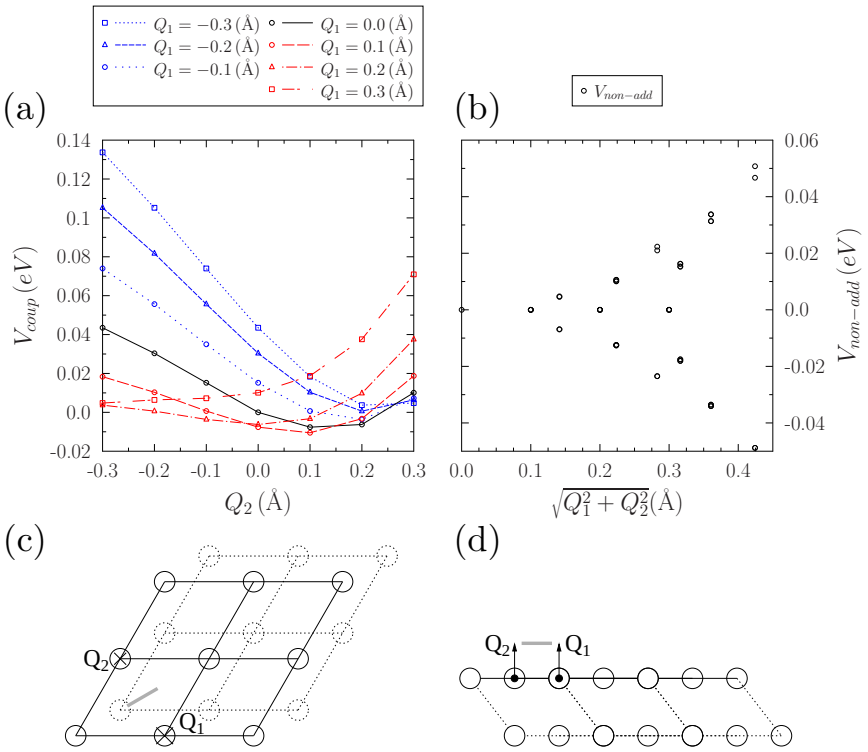

Figure 3.2: (a) shows V_{coup} for displacements along $\vec{Q}_1$ and $\vec{Q}_2$ where black, red and blue show no, a positive and a negative displacement along $\vec{Q}_1$ respectively. The displacements $\vec{Q}_1$ and $\vec{Q}_2$ are defined in (c) and (d) by showing a top and front view of the system respectively, where Cu atoms are indicated using circles and H_2 by the gray bar. (b) shows the non-additivity (see eq. 3.12) of the coupling potentials presented in (a). Q_1 and Q_2 in (a) and (b) refer to the magnitudes $|\vec{Q}_1|$ and $|\vec{Q}_2|$ respectively while Q_1 and Q_2 in (c) and (d) are the vectors $\vec{Q}_1$ and $\vec{Q}_2$.

on dynamics due to the large mass difference between H_2 and D_2 with Cu as well as the high velocities and consequent short interaction time of H_2.

The configuration with the most favorable coupling potential in figure 3.2, at -10.5 meV, is when both atoms are displaced by +0.1 Å along $\vec{Q}_1$ and $\vec{Q}_2$. When only one

atom is displaced while the other is at its ideal lattice position, the coupling potential is 7.5 meV. From a perspective where only additive interactions are considered (see eq. 3.7), this cannot be explained as both surface atoms should then interact independently. This means that a three (or more)-body interaction is present, or in other words: there is non-additivity of the coupling potential due to the surface displacements of two or more Cu atoms. The non-additivity of the coupling potential (see equation 3.10) is defined as the difference between the coupling potential of displacements $\overrightarrow{Q}_1$ and $\overrightarrow{Q}_2$ with the sum of the coupling potentials of only $\overrightarrow{Q}_1$ and only $\overrightarrow{Q}_2$ as given by

$$\begin{aligned} V_{nonadd}(\overrightarrow{r}, \overrightarrow{q}^{id} \rightarrow \overrightarrow{q}^{id} + \overrightarrow{Q}_1 + \overrightarrow{Q}_2) = \\ V_{coup}(\overrightarrow{r}, \overrightarrow{q}^{id} \rightarrow \overrightarrow{q}^{id} + \overrightarrow{Q}_1 + \overrightarrow{Q}_2) \\ -V_{coup}(\overrightarrow{r}, \overrightarrow{q}^{id} \rightarrow \overrightarrow{q}^{id} + \overrightarrow{Q}_1) \\ -V_{coup}(\overrightarrow{r}, \overrightarrow{q}^{id} \rightarrow \overrightarrow{q}^{id} + \overrightarrow{Q}_2). \end{aligned} \tag{3.12}$$

While this non-additivity can never be modeled with an additive interaction there are good arguments to believe that they are not too important. First of all, the additive interaction can be fitted including the configurations with non-additivity, resulting in an effective non-additive interaction that takes into account the average non-additivity. The distribution of the non-additivity was found to have a mean of -0.5 meV and a standard deviation (SD) of 6.3 meV which means that on average the correct coupling potential should be reproduced only introducing a slightly bigger spread in the modeled coupling potentials. Furthermore, the configurations where there is a lot of non-additivity are when there are two specific surface atoms that both have a large displacement. While it is certainly true that a single displacement of such a magnitude is not extremely unlikely, having two such large displacements is even less common and therefore decreases the probability of sampling this error. Finally, in a realistic configuration of a non-ideal surface all surface atoms are displaced and combining this with the fact that the non-additivity introduces an error that is on average zero, there is an even smaller mean error under these realistic conditions. Even without these arguments, under these circumstances, the absolute mean error of this non-additivity is well within the accuracy one can expect for the underlying DFT.

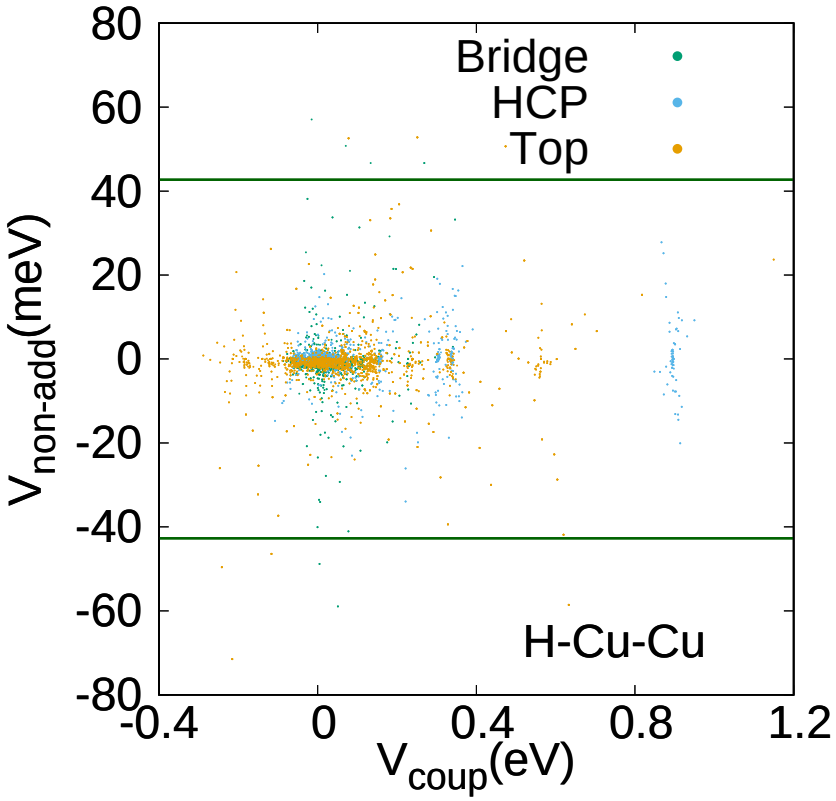

Figure 3.3: The non-additivity of V_{coup} is correlated to the value of V_{coup} for configurations with two surface atom displacements (H-Cu-Cu three-body interactions) and H_2 at the Bridge (green), HCP (blue) and Top (orange) site. The potential at which the non-additivity exceeds chemical accuracy is shown as a reference in dark green (these 43 meV lines correspond to more than 6 times the SD of the DFT data (6.3 meV))

In figure 3.3 a summary is presented of the coupling potentials and their respective non-additivity. The green lines are added as a reference to show the approximate accuracy of the underlying DFT method used. The behavior of the H-Cu-Cu non-

additivity is essentially independent of the chosen site (Bridge, HCP, Top) for H_2. Almost all coupling potentials of the H-Cu-Cu type have a non-additivity smaller than the accuracy of the DFT method, which means that any subsequent improvement of the fitting quality is not guaranteed to yield a more realistic coupling potential.

The H-H-Cu coupling potentials describe how the coupling potential changes when the H_2 bond distance changes ($\overrightarrow{r} \rightarrow \overrightarrow{r}'$) whilst also displacing a single Cu atom ($\overrightarrow{Q}$) at the same time. These coupling potentials were selected in a similar fashion as the H-Cu-Cu coupling potentials. Instead of selecting two surface atoms, only one was selected and the same displacements were used for the single atom in combinations with increasing and decreasing the H_2 bond distance from -0.3 Å until 0.3 Å with respect to the barrier position in steps of 0.1 Å. Other degrees of freedom of H_2 were sampled in the same way. Consequently, the H-H-Cu non-additivity is given by

$$\begin{aligned} V_{nonadd}(\overrightarrow{r} \rightarrow \overrightarrow{r}', \overrightarrow{q}^{id} \rightarrow \overrightarrow{q}^{id} + \overrightarrow{Q}) = \\ V_{coup}(\overrightarrow{r}', \overrightarrow{q}^{id} \rightarrow \overrightarrow{q}^{id} + \overrightarrow{Q}) \\ -V_{coup}(\overrightarrow{r}, \overrightarrow{q}^{id} \rightarrow \overrightarrow{q}^{id} + \overrightarrow{Q}) \\ -V_{coup}(\overrightarrow{r}', \overrightarrow{q}^{id} \rightarrow \overrightarrow{q}^{id}), \end{aligned} \tag{3.13}$$

where $V_{coup}(\overrightarrow{r}', \overrightarrow{q}^{id} \rightarrow \overrightarrow{q}^{id}) = 0$ due to the lack of surface displacements. The H-H distance r_{H-H} ranges from H_2 having dissociated at very large bond distances to the bond distance being so short that almost all available energy in the system has gone into this compression. Unlike the H-Cu-Cu interactions, the H-H-Cu interactions cannot be reproduced within chemical accuracy using a two-body H-Cu interaction. Figure 3.4 shows the non-additivity of the H-H-Cu coupling potentials and there is a much broader distribution with a mean of -5.0 meV and a SD of 74.6 meV, with some non-additivities being more than ten times chemical accuracy. Generally the non-additivity and coupling potential presented in this chapter are linearly dependent on the H_2-bond distance. Such linear dependence has been seen before for the vibrational coupling of diatomics interacting with atoms and other diatomics [34, 35]. In contrast to the H-Cu-Cu non-additivity, there is a slight difference of the H-H-Cu non-addivity for H_2 at different sites. There is a larger spread of the non-additivity for H_2 at the bridge

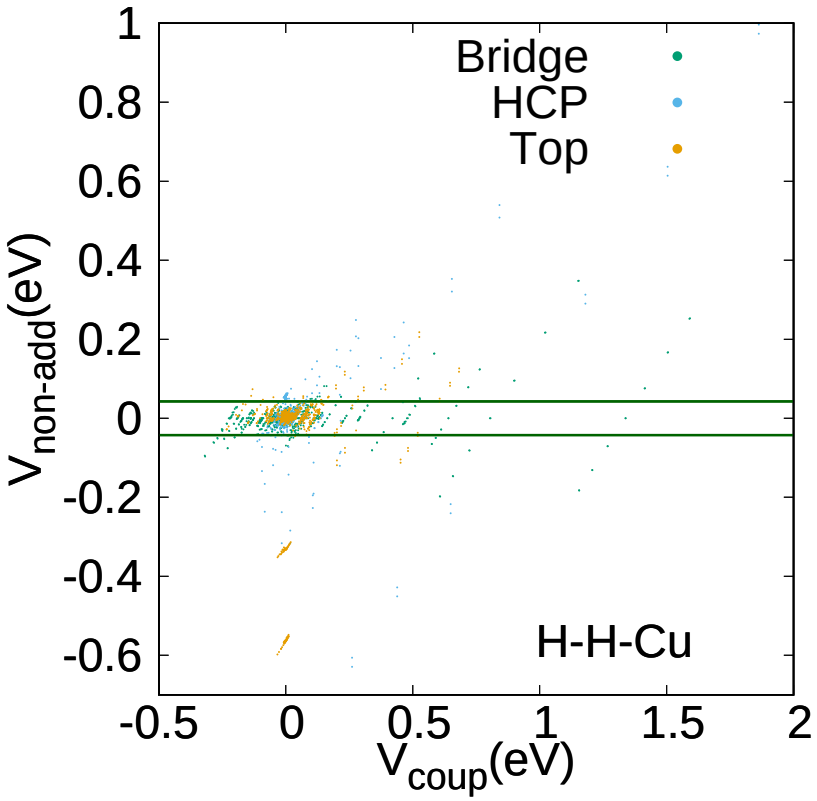

Figure 3.4: Same as Figure 3.3 but for configurations with one surface atoms displacement combined with the H-H bond not at the equilibrium distance (H-H-Cu three-body interactions).

site, while for some configurations at the top site there is a very large non-additivity, eventhough there is a small coupling potential. Due to the large non-additivity for H-H-Cu interactions, I conclude that it is necessary to make use of the H_2-bond adapted Rydberg function.

3.3.2 Parameters for the Static Corrugation Model

The coupling potential discussed in the two previous sections was fitted using the H_2-bond adapted Rydberg function using the fitting procedure described above.

All fits take the H-Cu-Cu interactions into account only effectively while the H-H-Cu interactions are taken into account through the r_{H-H} dependence of the parameters P (see equation 3.8). The fitting procedure was repeated with four different sets of constraints. First the most relaxed case where H-H-Cu three-body interactions are taken into account and two different sets of parameters were assigned, one for the first and one for the second surface layer copper atoms involved in the H-Cu interaction (3Body 2Layer). Then there is the case were a single set of parameters is used for both layers (3Body 1Layer) and the case where all non-additive interactions are taken into account only effectively (2Body 2Layer). Finally the fit was also performed constraining both the parameters to a single set and taking non-additive interactions into account only effectively (2Body 1Layer). This is thus essentially a refit of the old SCM [14] using the new and vastly extended set of DFT data set and consequent coupling potential. The best fit is for the 3Body 2Layer case with a close second place for the 3Body 1Layer case. The other two cases have a very similar RMSE as reported in literature for other methods such as the ReaxFF [36]. In the case of the H_2-bond adapted Rydberg function the plots are for several different H_2-bond distances as shown in table 3.3. An overview of the RMSE is presented in table 3.1 and the parameters for all 1Layer cases are given in table 3.2.

Table 3.1: An overview of the different fitting constraints and the corresponding names.

Fit	3 Body interactions	Different parameter sets	RMSE (meV)
3Body 2Layer	Yes	Yes	29.4
2Body 2Layer	No	Yes	62.4
3Body 1Layer	Yes	No	42.7
2Body 1Layer	No	No	66.6

Table 3.2: Fitted SCM Parameters where units of length are in Bohr and units of Energy in Hartree. Columns a and b for the 3-body interactions refer to $P_{i,a}$ and $P_{i,b}$ from equation 3.8.

	Ref. [14]	2-body	3-body	
			b	a
P_0	-0.0303	-0.0339	-0.0704	0.0166
P_1	0.1035	0.1024	0.0235	0.0287
P_2	-0.0692	-0.0802	-0.0633	-0.0072
P_3	-	0.0111	0.0272	-0.0064
P_4	2.3005	2.3023	2.2897	0.0236
P_5	1.2744	1.2929	1.2910	-0.0031
P_6	7.4442	7.4400	7.4402	0.0008
P_7	7.4636	10.4600	10.4601	0.0000

Comparing the V_{H-Cu} interaction from previous work [14] with the 2Body 1Layer fit to the new DFT data set in figure 3.5 the interaction is weaker than before but qualitatively very similar. The position of the maximum is shifted to about half a Bohr shorter H-Cu distance while the position of the well is still the same. When instead the fit is performed with different parameters for different layers, the first layer interaction is shifted to a lower energy but the barrier and equilibrium position are still very similar in position and height. The second layer interaction on the other hand becomes much more repulsive at low distance and slightly more attractive at high distances. It should be noted here that the repulsive wall is not a regime that is sampled as it is not possible for an H atom to get this close to a second layer atom. The three-body interaction is represented in figure 3.5 by showing the energy dependence of the H-Cu distance at several fixed values of the H-H distance as discussed in table 3.3 (green curves). The general shape of the interaction is the same at every H-H distance but at high H-H distances the barrier is much higher while the well is much lower in energy. There is also a slight broadening effect, such that the well is shifted to smaller H-Cu distances and the barrier to larger H-Cu distances. At very small H-H

Table 3.3: An overview of the different H-H distances used in this section

Name	H-H Distance (Å)
Bridge	1.025
HCP	1.547
Top	1.402
Lowest (r_{min})	0.725
Highest (r_{max})	1.847

distances, the V_{H-Cu} interaction becomes almost completely repulsive. Surprisingly, the bridge site, which has the lowest H-H distance and therefore the most repulsive H-Cu interaction, actually has the lowest barrier for reaction. These two statements are not contradictory because the H-Cu interaction only includes the influence of the H-H distance on V_{coup} and not the H-H interaction itself, which is included in the CRP potential (V_{CRP}). The described features suggest that the fitted potential is at least qualitatively in agreement with the properties of the PES and the RMSE suggests that there is also a quantitative agreement.

While the RMSE of the 3-body 2-layer fit suggests it is the best fit, the shape of the V_{H-Cu} interaction potential tells a different story. The problem in this case is the fit coverage: there are almost no first layer interactions in the 8 to 10 Bohr region so there is no constraint on the fitting procedure to keep the V_{H-Cu} interaction at a sensible value. Dynamical calculations using the underfitted 3-body 2-layer V_{H-Cu} yielded non-sensible results and are not presented in this work.

Henceforth in this chapter only a single set of parameters used for both the first and second layer H-Cu interaction is considered instead. Using that fitting procedure to fit the new set of coupling potentials this chapter presents a successfully fitted H_2-bond adapted Rydberg function. The resulting RMSE of the 3-body 1-layer fit is significantly improved compared to the RMSE of the SCM from previous work [14] when applied to the new DFT data set and is within the same accuracy as the DFT data used for the fitting.

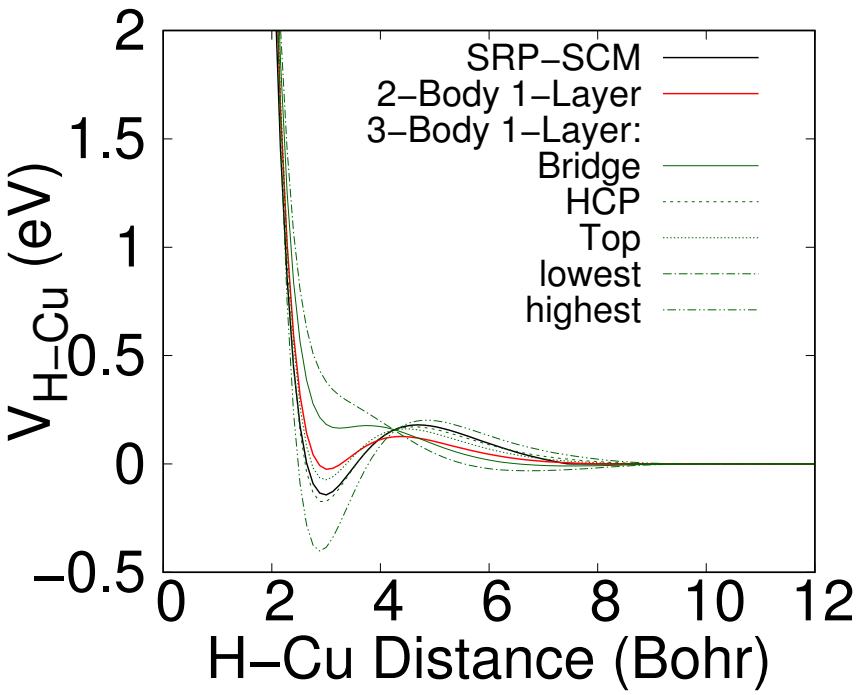

Figure 3.5: The V_{H-Cu} interaction is shown as a function of the H-Cu distance r_{H-Cu} for the SCM from Ref. [14] (black), the 2-body 1-layer fit (red) and the 3-body 1-layer fit (green) . The three-body interaction is represented by showing the potential dependence on the H-Cu distance at specific H-H distances according to table 3.3.

3.3.3 Dynamics on Different Potential Energy Surfaces

To properly compare the newly developed SCM with the previous SCM [14], which use two comparable but slightly different DFT functionals, a comparison between the results using the 6D CRP interpolations (BOSS) for the two used functionals is presented first. The previous SCM used the SRP functional by Díaz et al. [16], for which the CRP interpolation is refered to with SRP-BOSS (in red) in this chapter and the newly developed SCM uses the SRP48 functional by Nattino et al. [37] for which a CRP interpolation SRP48-BOSS (in black) was made by Mondal et al. [17]. Using these two

different PESs, dynamical scattering simulations were performed for D_2 on Cu(111). While reaction probabilities have been reported before, the rovibrationally (in)elastic scattering probabilities have not. Only the initial rovibrational states (v=0, J=0), (v=0, J=11) and (v=1, J=6) are discussed here specifically and a general overview is given for the other states computed (for which the results are available digitally).

The general trend for QC reaction probabilities of D_2 on Cu(111) is that at low incidence energies there is no reaction and as the incidence energy increases the reaction probability increases until it reaches a maximum value called the saturation value. As described previously [10], the general curve of the reaction probability can be described with a modified logistics function. When there is no reaction, there can either be elastic scattering or inelastic scattering. At low incidence energies the elastic scattering dominates as there is not yet enough energy or coupling available to cause a rovibrational excitation while at high energies the inelastic scattering dominates as there is more coupling due to the corrugation and anisotropies close to the surface. It is also possible for the H_2 molecule to change its momentum along the surface lattice vectors when scattering, which is called diffraction. The effect of diffraction was not considered in the sense that the reported observables are summed over the final diffraction states.

The differences between the reaction and (in)elastic scattering probabilities predicted by the two PESs (see black and red curves in fig. 3.6) are dependent on the rovibrational state. For the (v=0, J=0) state the reaction and (in)elastic scattering probabilities are different below 0.9 eV while for the (v=0,J=0) state the reaction and (in)elastic scattering probabilities are different above 0.5 eV and for the (v=1,J=6) state the reaction probabilities are the same for all energies whereas the (in)elastic scattering probabilities deviate below 0.5 eV.

The reaction and rovibrationally (in)elastic scattering probabilities for the (v=0, J=0) initial state are shown in figure 3.6a and discussed in detail first. For incidence energies above 0.9 eV, the probabilities are almost the same for the two PESs. The probabilities for elastic scattering are the same above 0.7 eV while the reaction probability is lower in the case of the SRP-BOSS PES and the inelastic scattering probabilities are

higher. This means that in the region of 0.7 eV to 0.9 eV there is a different preference to either react or scatter for the SRP48-BOSS PES compared to the SRP-BOSS PES. In the case of the SRP48-BOSS PES, the preference is more towards reaction, while in the case of the SRP-BOSS PES the incidence energy is converted into some rovibrational excitations and the preference is towards rovibrationally inelastic scattering. At even lower incidence energies the rovibrationally inelastic scattering probability for the SRP-BOSS PES is lower only for the lowest incidence energy, for all other incidence energies it is higher than the rovibrationally inelastic scattering probability of the SRP48-BOSS PES.

For the rotationally excited state (v=0, J=11), as shown in figure 3.6b, there is almost no difference between the two PESs except for a small broadening of the reaction probability in the case of the SRP-BOSS PES compared to the SRP48-BOSS PES. The lower reaction probability is mostly compensated by a higher inelastic scattering for the SRP-BOSS PES.

On the other hand, the two PESs yield very similar reaction probabilities for the vibrationally excited state (v=1, J=6) while the SRP-BOSS PES inelastic and elastic scattering probability curves cross earlier compared to the SRP48-BOSS PES as shown in figure 3.6c . The general trend of all computed rovibrational states is that as more vibrational energy is added, the reaction probabilities become almost identical between the SRP48-BOSS and SRP-BOSS PES while adding more rotational energy causes the elastic and inelastic scattering probabilities to be more comparable.

Here the argument is that these two effects are distinct features of the PESs based on a normal mode analysis performed along the minimum energy path (MEP) for both PESs as given Sec. 3.A. The difference between the widths of the reaction probabilities for the SRP and SRP48 are mostly determined by how much vibrational energy (in r) is added initially in H_2. If vibrational energy is added, the details of the intrinsic curvature (or how the forces along Z and r change) of the PES along the MEP towards the barrier becomes less important because there is more energy available. The (extrinsic) curvature describing the geometric shape of the reaction path is essentially identical for the two PESs. We note that both functionals yield very similar barrier

heights and locations for this system as well as near identical MEPs. Therefore, it could be argued that it is the intrinsic curvature, constrained in r and Z, that determines the different reaction probability widths for the SRP-BOSS and SRP48-BOSS. Previously it has been reported [38] that the energetic corrugation can also have an influence on the reaction probability width, but that would not directly explain the strong dependence on the initial vibrational state. If instead rotational energy is added, the intrinsic curvature, in r and Z, of the PES towards the barrier is still important. A similar argument can be made for the energy at which the rovibrationally elastic and inelastic scattering probability curves cross, where it is mostly the anisotropy in θ and ϕ that determines if the rovibrational state changes. If the molecule is rotating relatively fast, it feels an 'average' of the potential in θ and therefore the exact shape of PES becomes less important.

Both PESs were designed to reproduce molecular beam experiments, where the effective barrier height is the most important property of the PES, but if there is not enough energy available to sample the effective barrier, the shape of the PES towards the barrier is also important.

3.3.4 Comparison of Different Static Corrugation Models

In this section a comparison is made between the new SCM based on the 6D PES from Mondal et al. [17] and the newly fitted coupling potential (SRP48-SCM3B), and a SCM from previous work [14] based on the PES from Diaz et al. [16] (SRP-SCM). Both SCMs were computed for a surface temperature of 925K including both surface displacements and surface expansion as described previously in this chapter and Chap. 2.

Figure 3.6a shows the effect of using the SCM compared to the BOSS model for the rovibrational ground state (v=0, J=0). For the SRP-SCM PES, there is a large broadening [9, 14, 39] of the reaction probability at both low and high reaction probabilities while the SRP48-SCM3B PES only shows increased reaction probabilities at low incidence energies. The reaction probability of the SRP48-SCM3B PES starts to increase earlier compared to SRP-SCM, but after 0.8 eV of incidence energy, the slope

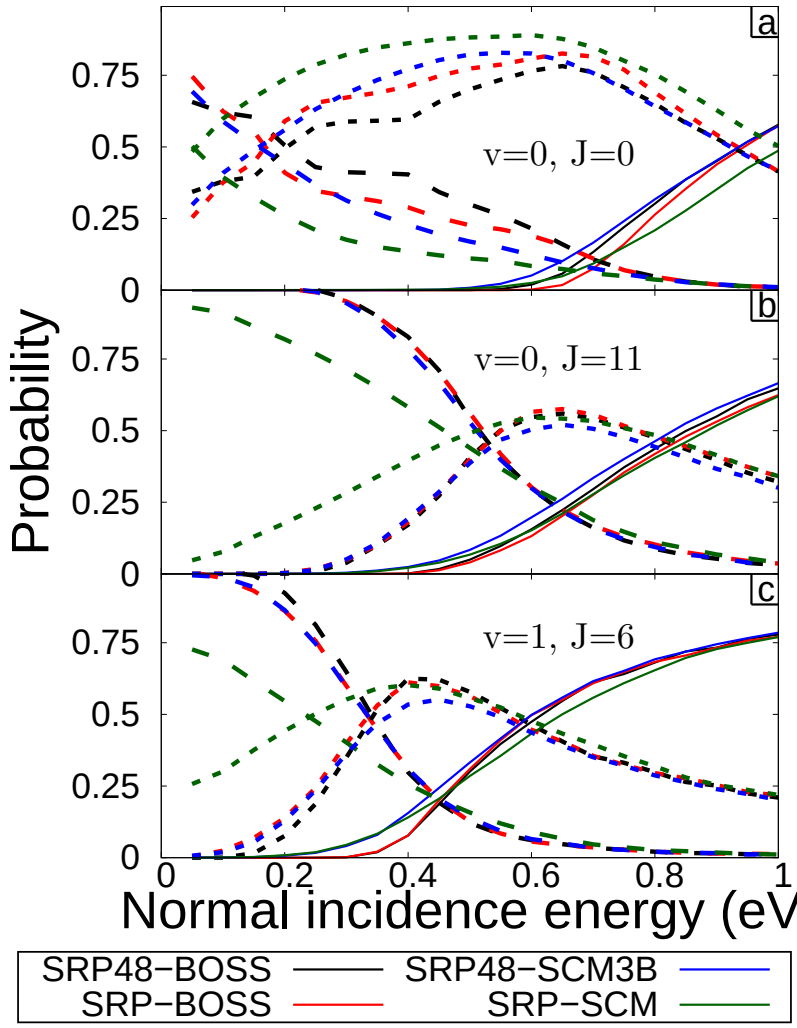

Figure 3.6: The state-specific reaction (solid), elastic scattering (long dash) and inelastic scattering (short dash) probabilities are shown as a function of the incidence energy for SRP48-BOSS (black), SRP48-SCM3B (blue), SRP-BOSS (red) and SRP-SCM (green). (a), (b) and (c) show the (v=0, J=0), (v=0,J=11) and (v=1,J=6) rovibrational state-specific reaction and (in)elastic scattering probabilities respectively.

is essentially the same as for the SRP-SCM PES. The rovibrationally elastic and inelastic scattering probability curves for the SCM PESs are smoother and do not show sudden changes of the slope as is shown e.g. in the SRP48-BOSS results (black) at 0.4 eV. In the case of SRP-SCM, the rovibrationally inelastic scattering is significantly larger for all incidence energies.

Figure 3.6b shows the result for the rotationally excited (v=0, J=11) state. Here the crossing point of the elastic and inelastic rovibrationally scattering probabilities is the same for SRP-BOSS, SRP48-BOSS and SRP48-SCM3B while SRP-SCM is different. For the (v=1, J=6) state in figure 3.6c the same difference between the SRP-SCM and the others is observed. While the SRP48-BOSS, SRP48-SCM3B and SRP-BOSS PESs are all similar at high incidence energies, when sampling the corrugation close to the Cu(111) surface, the SRP-SCM PES is still different between an incidence energy of 0.4 and 0.9 eV. Furthermore, the rovibrationally inelastic scattering probability is orders of magnitude higher for very low incidence energies.

The general effect of adding the SCM to both the previously discussed PESs seems to be a broadening in the reaction probability, as well as a larger fraction of rovibrationally inelastic scattering at low energies compared to the BOSS model. The biggest difference between the SRP-SCM and new SRP48-SCM3B is that the new SRP48-SCM3B follows the same trend as the BOSS models if the initial rovibrational state is changed, while the SRP-SCM does not. The broadening effect of the SRP-SCM is in general bigger than that of the SRP48-SCM3B.

The differences between the SRP-SCM and SRP48-SCM3B PESs of the broadening behaviour are hard to attribute to differences in DFT methods used, because the SRP-BOSS PES has the same behaviour as both SRP48 PESs with respect to this behaviour. There are three possible explanations for the difference between the SCMs. First of all the SRP48-SCM3B is fitted to almost 100 times more DFT configurations and also includes displacements of two surface atoms. Secondly, the coupling potential used in the SRP-SCM had a short cut-off in the H-Cu distance that prevented almost all contributions due to second layer displacements. It is known from the work of Bonfanti et al. [40] that the second layer displacements are very important for the

barrier heights. Finally there are H-H-Cu three-body terms included in the SRP48-SCM3B which are, as argued before, not negligible and are not included in the purely additive and pair-potential based SRP-SCM.

3.3.5 Comparing with AIMD and Experimental Results

When comparing the computed reaction probabilities from the BOSS model and SCM with results from AIMD [10] in figures 3.7a, b and c, there is a very good agreement across all incidence energies. This was to be expected as the SCM accurately reproduces the DFT used directly by AIMD. Differences are attributed to statistical errors due to the small amount of trajectories in AIMD, the periodicity of the surface displacements in AIMD, the relatively large time step in AIMD, the lack of energy exchange with the lattice with the SCM, and deviation of the SCM from DFT (42.7 meV RMSE). The reaction probability curves can be considered to be equivalent, which is extremely useful because it allows to select the correct DFT functional by comparing to experiments at elevated surface temperature using the SCM method. This is orders of magnitude computationally cheaper than AIMD. Figure 8 in Ref. [10] shows that essentially no desorbed molecules with a COM kinetic energy higher than 0.7 eV are measured during the experiment. Therefore only experimental results up to an indicence energy of 0.7 eV are considered for determining the accuracy of the theoretical models. With that in mind, the rotational and vibrational excited states, shown in figure 3.7b and c respectively, are reproduced very well by the theory. The rovibrational ground state, in figure 3.7a, on the other hand is not. This can be understood due the (v=0, J=0) state being much more sensitive to the shape of the PES around and towards the barrier rather than only the dynamical barrier height as discussed before. Similar to the argument on the accuracy of the SCM fit, an argument can be made here that further improvements in the dynamical model will only lead to a better accuracy when a more accurate DFT functional is found.

3.3.6 Initial Rovibrational State Dependence of the Reaction Probability

The computed reaction probabilities have been fitted using a generalized logistics function (GLF) [10] for all available rovibrational states. There are two important parameters from this fit, the inflection point (E_0) and the width of the curve. The inflection point is where the growth of the reaction probability first starts to decrease, which would be the energy at which the reaction probability is half of its maximum, if the reaction probability would be symmetrical with respect to the inflection point. There is however, a small deviation from this symmetry. Note that there are several different definitions of E_0 in literature, depending on the chosen fitting function, and that should be considered when comparing E_0 values from this work. The width is a measure of how broad the reaction probability curve is and is known to increase when taking into account surface temperature effect [10, 14]. I was not able to compute the uncertainties in the fitted E_0 and width parameters. Comparison with AIMD and experimental results remain difficult. For AIMD, the limited number of data points in incidence energy, due to the high computational effort, limits the fitting quality of the GLF. On the other hand, the GLF fits to experiments are based on time-of-flight (ToF) measurements of desorption experiments that are subsequently converted to reaction probabilities making use of detailed balance. Here the absolute saturation values are obtained from other molecular beam experiments. The consequences of fitting experimental results in such a way and comparing with theory have recently been discussed [41]. Figure 3.8a and b show the fitted E_0 parameters for v=0 and v=1 at increasing J. For all rovibrational states, the SRP-BOSS and SRP48-BOSS are in very close agreement, even though there is a small difference between the two PESs as discussed above. While the SRP-SCM predicts the same E_0 as the two BOSS models for J larger than 6, both for v=0 and v=1, and a higher E_0 at lower J, the SRP48-SCM3B predicts lower E_0 values except for v=1 and J=0 or J=1. For v=0 the experimental and AIMD results are in reasonable agreement while for v=1 there is a discrepancy between experimental and all theoretical results for J smaller than 3. It is not clear whether

this discrepancy is due to a failure of the theoretical models or because of the way the experimental results have been fitted. On the other hand, the width parameters in figures 3.8c and d show a large dependence on which SCM was used. The width parameters for both SRP-BOSS and SRP48-BOSS are between 0.1 and 0.18 eV and very similar. Including the SCM then increases the width, by approximately 0.05 eV in the case of SRP48 and 0.1 eV in the case of SRP. The AIMD results are in agreement with the increased width of the SRP48-SCM3B while the SRP-SCM predicts a larger increase in the width. While there is a good agreement between the experimental results and the SRP-SCM for v=0, it is very unlikely that this is due to the quality of the fit, considering the fact that AIMD is not able to reproduce the large widths found in the experiment. Overall, the new SRP48-SCM3B accurately reproduces AIMD results based on the fitted E_0 and width parameters.

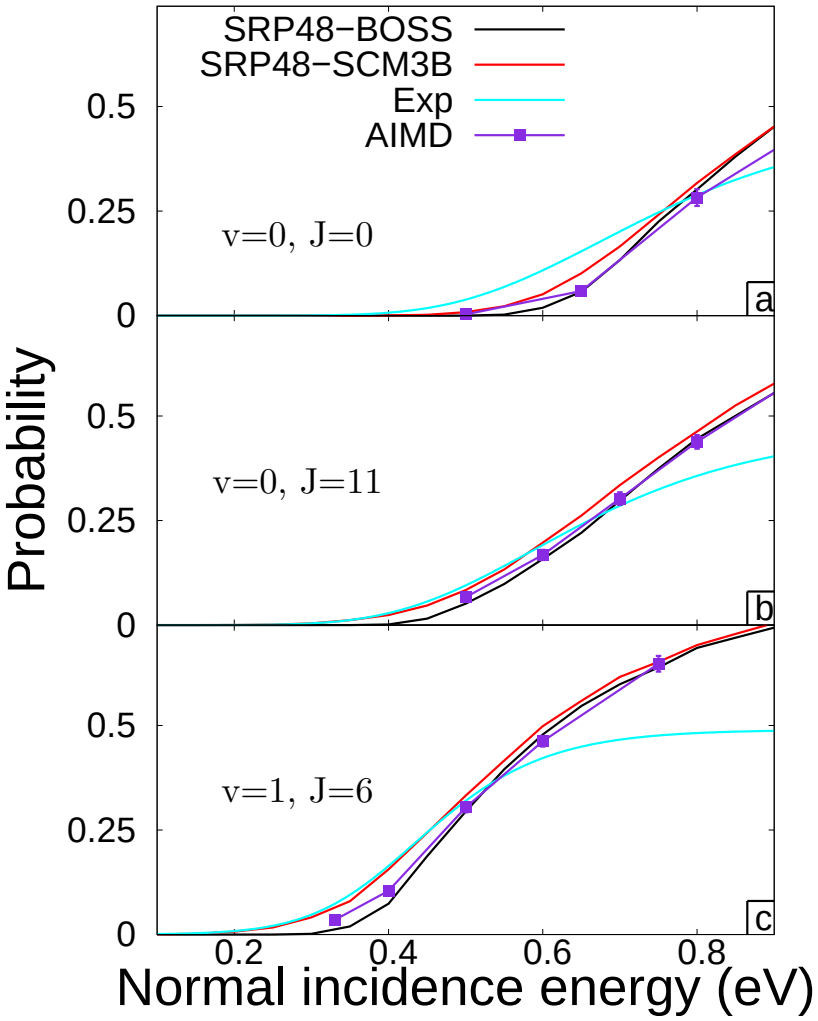

Figure 3.7: State-specific reaction probabilities are shown as a function of incidence energy at normal incidence for SRP48-BOSS (black), SRP48-SCM3B (red), AIMD with SRP48 from Ref. [10] (purple) while a fit to the time-of-flight data of experimental results taken from Ref. [10] are shown in cyan. (a), (b) and (c) show the (v=0, J=0), (v=0,J=11) and (v=1,J=6) rovibrational state-specific reaction probabilities respectively.

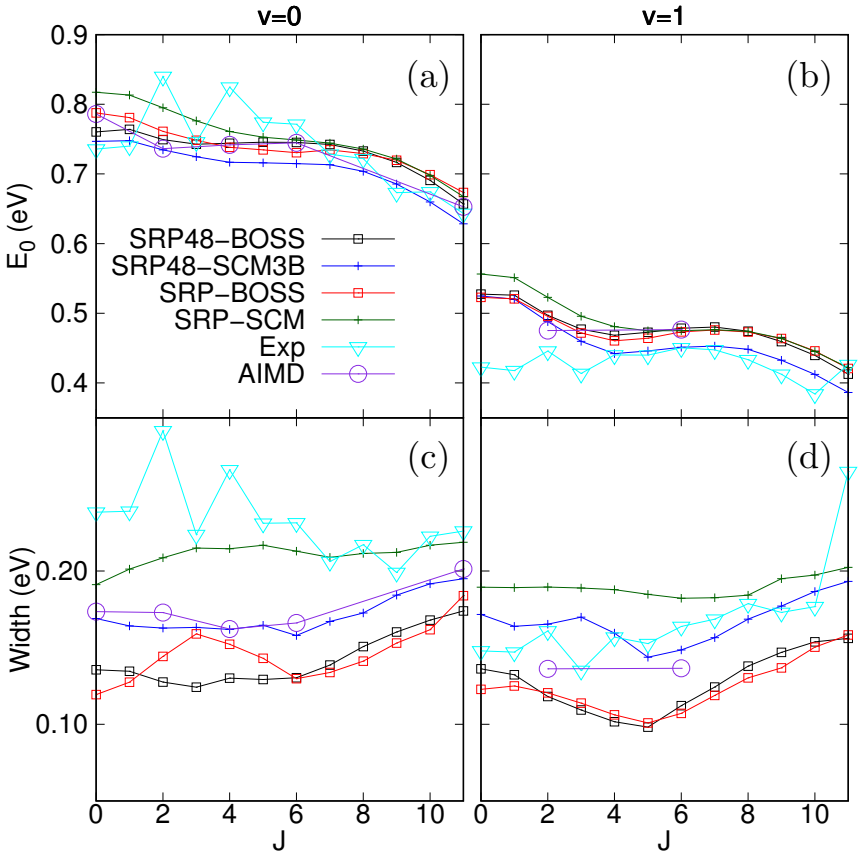

Figure 3.8: (a) and (b) show the fitted inflection point E_0 as a function of the rotational state J for vibrational state v=0 and v=1 respectively. (c) and (d) show the fitted width as a function of the rotational state J for vibrational state v=0 and v=1 respectively. The black and blue curves are obtained by fitting state-specific reaction probabilities, which were presented in this chapter, for SRP48-BOSS and SRP48-SCM3B respectively. Red and green curves are likewise obtained by refitting the data from Ref. [14] using the GLF. The cyan triangles and purple circles are obtained from Ref. [10] where the experimental (cyan triangles) results are obtained by fitting state-specific time-of-flight data and the AIMD (purple circles) results are obtained by fitting state-specific reaction probabilities.

3.4 Conclusions

A new coupling potential has been fitted for H_2 on Cu(111) within the SCM framework based on the SRP48 density functional using the same setup as AIMD calculations [10]. A large database of coupling potentials has been constructed for H_2 on Cu(111) at several high symmetry sites for a large amount of surface displacements. Included are configurations with two surface displacements, capturing the H-Cu-Cu three-body interactions which were found to have a negligible non-additivity. In contrast, configurations corresponding to one surface displacements and variable H_2 bond distance, describing the H-H-Cu three-body interactions, show a large non-additivity and can therefore not be described accurately using the two-body SCM. The functional form of the coupling potential has thus been extended to have a H_2 bond distance dependence of the Rydberg parameters, including H-H-Cu three-body interactions explicitly. Simulations of state-specific desorption experiments using the BOSS model show that the SRP and SRP48 PES are essentially identical, except for the reaction and scattering of rovibrational ground-state H_2 even though both functionals were constructed to reproduce the same molecular beam experiments. The differences between the PESs could not be accounted for by the barrier heights, extrinsic curvature of the MEP or zero point vibrational energy but are instead attributed to the intrinsic curvature of the PES along the MEP. Using the newly developed SCM based on the SRP48 AIMD and experimental results were succesfully reproduced and consequently the SCM can be a good substitute for AIMD in the case of H_2 on Cu(111). For heavier molecules on metal surfaces, where surface motion can be important and the SCM may not be suitable (due to the increased amount of expected energy exchange with the surface), it will be interesting to use a strain potential to describe the PES of a clean surface using e.g. embedded atom potentials [42–45]. Combining this strain potential with the coupling potential yields a full dimensional PES that allows energy exchange with the surface.

3.A Comparison of Minimum Energy Paths of H_2 on Cu(111) for SRP and SRP48

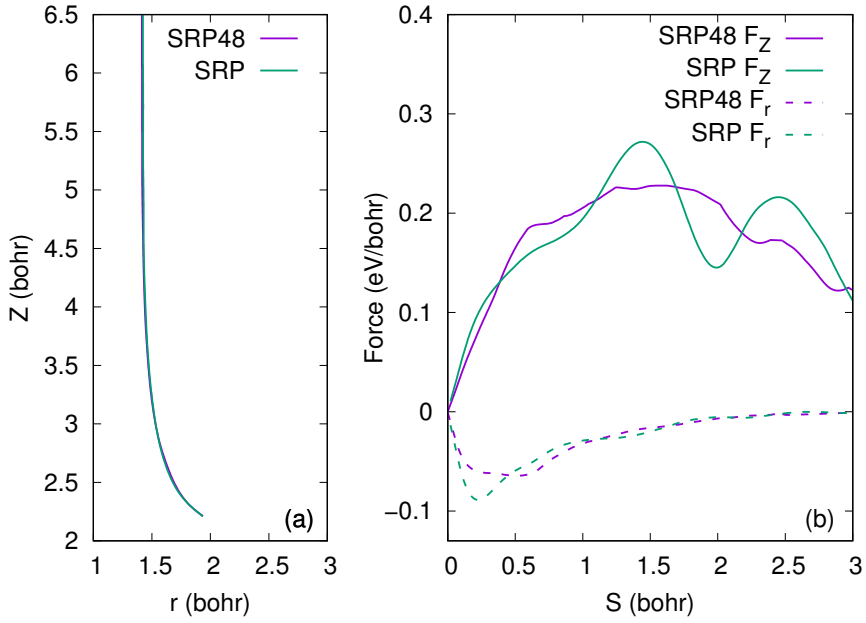

Figure 3.9: (a) shows the MEP until the barrier on the bridge site for the SRP48 and SRP PES in purple and green respectively. (b) shows the forces in Z (solid) and r (dashed) along the same MEP for SRP48 (purple) and SRP (green). S=0 bohr corresponds the barrier position.

In figure 3.9a, the minimum energy paths of both the SRP48 and SRP functional are shown to be essentially identical. In contrast, the forces along Z and r are slightly different in figure 3.9b. The difference in the force along Z between SRP and SRP48 for large S (far away from the transition state) are not important for the dynamics because there is only a small force along r and thus very little coupling between the two. On the other hand, the small differences at low S (below 1.5 Å) show that there indeed is a difference in intrinsic curvature around the minimum energy path even though the

minimum energy paths are essentially identical.

References

[1] P. Spiering, M. Wijzenbroek, and M. F. Somers. "An Improved Static Corrugation Model". In: *J. Chem. Phys.* 149 (2018), p. 234702. DOI: 10.1063/1.5058271.

[2] G. Ertl. "Reactions at Surfaces: From Atoms to Complexity (Nobel Lecture)". In: *Angew. Chem. Int. Edit.* 47 (2008), pp. 3524–3535. DOI: 10.1002/anie.200800480.

[3] T. Zambelli, J. V. Barth, J. Wintterlin, and G. Ertl. "Complex Pathways in Dissociative Adsorption of Oxygen on Platinum". In: *Nature* 390 (1997), pp. 495–497. DOI: 10.1038/37329.

[4] H. A. Michelsen, C. T. Rettner, and D. J. Auerbach. "On the Influence of Surface Temperature on Adsorption and Desorption in the D_2/Cu(111) System". In: *Surf. Sci.* 272 (1992), pp. 65–72. DOI: 10.1016/0039-6028(92)91422-8.

[5] H. A. Michelsen, C. T. Rettner, and D. J. Auerbach. "State-Specific Dynamics of D_2 Desorption from Cu(111): The Role of Molecular Rotational Motion in Activated Adsorption-Desorption Dynamics". In: *Phys. Rev. Lett.* 69 (1992), pp. 2678–2681. DOI: 10.1103/PhysRevLett.69.2678.

[6] C. T. Rettner, D. J. Auerbach, and H. A. Michelsen. "Observation of Direct Vibrational Excitation in Collisions of H_2 and D_2 with a Cu(111) Surface". In: *Phys. Rev. Lett.* 68 (1992), pp. 2547–2550. DOI: 10.1103/PhysRevLett.68.2547.

[7] C. T. Rettner, H. A. Michelsen, and D. J. Auerbach. "Determination of Quantum-State-Specific Gas—Surface Energy Transfer and Adsorption Probabilities as a Function of Kinetic Energy". In: *Chem. Phys.* 175 (1993), pp. 157–169. DOI: 10.1016/0301-0104(93)80235-2.

[8] C. T. Rettner, H. A. Michelsen, and D. J. Auerbach. "Quantum-State-Specific Dynamics of the Dissociative Adsorption and Associative Desorption of H_2 at a Cu(111) Surface". In: *J. Chem. Phys.* 102 (1995), pp. 4625–4641. DOI: 10.1063/1.469511.

[9] M. J. Murphy and A. Hodgson. "Adsorption and Desorption Dynamics of H2 and D2 on Cu(111): The Role of Surface Temperature and Evidence for Corrugation of the Dissociation Barrier". In: *J. Chem. Phys.* 108 (1998), pp. 4199–4211. DOI: 10.1063/1.475818.

[10] F. Nattino, A. Genova, M. Guijt, A. S. Muzas, C. Díaz, et al. "Dissociation and Recombination of D_2 on Cu(111): Ab Initio Molecular Dynamics Calculations and Improved Analysis of Desorption Experiments". In: *J. Chem. Phys.* 141 (2014), p. 124705. DOI: 10.1063/1.4896058.

[11] G.-J. Kroes. "Towards Chemically Accurate Simulation of Molecule-Surface Reactions". In: *Phys. Chem. Chem. Phys.* 14 (2012), pp. 14966–14981. DOI: 10.1039/C2CP42471A.

[12] C. Díaz, E. Pijper, R. A. Olsen, H. F. Busnengo, D. J. Auerbach, et al. "Chemically Accurate Simulation of a Prototypical Surface Reaction: H2 Dissociation on Cu(111)". In: *Science* 326 (2009), pp. 832–834. DOI: 10.1126/science.1178722.

[13] D. A. McCormack, G.-J. Kroes, E.-J. Baerends, and R. C. Mowrey. "Six-Dimensional Quantum Dynamics of Dissociation of Rotationally Excited H_2 on Cu(100)". In: *Faraday Discuss.* 110 (1998), pp. 267–285. DOI: 10.1039/A804213F.

[14] M. Wijzenbroek and M. F. Somers. "Static Surface Temperature Effects on the Dissociation of H2 and D2 on Cu(111)". In: *J. Chem. Phys.* 137 (2012), p. 054703. DOI: 10.1063/1.4738956.

[15] R. A. Olsen, H. F. Busnengo, A. Salin, M. F. Somers, G.-J. Kroes, et al. "Constructing Accurate Potential Energy Surfaces for a Diatomic Molecule Interacting with a Solid Surface: H_2+Pt(111) and H_2+Cu(100)". In: *J. Chem. Phys.* 116 (2002), pp. 3841–3855. DOI: 10.1063/1.1446852.

[16] C. Díaz, R. A. Olsen, D. J. Auerbach, and G.-J. Kroes. "Six-Dimensional Dynamics Study of Reactive and Non Reactive Scattering of H2 from Cu(111) Using a Chemically Accurate Potential Energy Surface". In: *Phys. Chem. Chem. Phys.* 12 (2010), pp. 6499–6519. DOI: 10.1039/C001956A.

[17] A. Mondal, M. Wijzenbroek, M. Bonfanti, C. Díaz, and G.-J. Kroes. "Thermal Lattice Expansion Effect on Reactive Scattering of H2 from Cu(111) at Ts = 925 K". In: *J. Phys. Chem. A* 117 (2013), pp. 8770–8781. DOI: 10.1021/jp4042183.

[18] P. Spiering and J. Meyer. "Testing Electronic Friction Models: Vibrational De-Excitation in Scattering of H_2 and D_2 from Cu(111)". In: *J. Phys. Chem. Lett.* 9 (2018), pp. 1803–1808. DOI: 10.1021/acs.jpclett.7b03182.

[19] A. C. Luntz and M. Persson. "How Adiabatic Is Activated Adsorption/Associative Desorption?" In: *J. Chem. Phys.* 123 (2005), p. 074704. DOI: 10.1063/1.2000249.

[20] K. Shakouri, J. Behler, J. Meyer, and G.-J. Kroes. "Accurate Neural Network Description of Surface Phonons in Reactive Gas–Surface Dynamics: N_2 + Ru(0001)". In: *J. Phys. Chem. Lett.* 8 (2017), pp. 2131–2136. DOI: 10.1021/acs.jpclett.7b00784.

[21] J. Behler, S. Lorenz, and K. Reuter. "Representing Molecule-Surface Interactions with Symmetry-Adapted Neural Networks". In: *J. Chem. Phys.* 127 (2007), p. 014705. DOI: 10.1063/1.2746232.

[22] B. Kolb, X. Luo, X. Zhou, B. Jiang, and H. Guo. "High-Dimensional Atomistic Neural Network Potentials for Molecule–Surface Interactions: HCl Scattering from Au(111)". In: *J. Phys. Chem. Lett.* 8 (2017), pp. 666–672. DOI: 10.1021/acs.jpclett.6b02994.

[23] Y. Zhang and W. Yang. "Comment on "Generalized Gradient Approximation Made Simple"". In: *Phys. Rev. Lett.* 80 (1998), pp. 890–890. DOI: 10.1103/PhysRevLett.80.890.

[24] B. Hammer, L. B. Hansen, and J. K. Nørskov. "Improved Adsorption Energetics within Density-Functional Theory Using Revised Perdew-Burke-Ernzerhof Functionals". In: *Phys. Rev. B* 59 (1999), pp. 7413–7421. DOI: 10.1103/PhysRevB.59.7413.

[25] G. Kresse and J. Hafner. "*Ab Initio* Molecular-Dynamics Simulation of the Liquid-Meta— Amorphous-Semiconductor Transition in Germanium". In: *Phys. Rev. B* 49 (1994), pp. 14251–14269. DOI: 10.1103/PhysRevB.49.14251.

[26] G. Kresse and J. Furthmüller. "Efficient Iterative Schemes for Ab Initio Total-Energy Calculations Using a Plane-Wave Basis Set". In: *Phys. Rev. B* 54 (1996), pp. 11169–11186. DOI: 10.1103/PhysRevB.54.11169.

[27] D. Vanderbilt. "Soft Self-Consistent Pseudopotentials in a Generalized Eigenvalue Formalism". In: *Phys. Rev. B* 41 (1990), pp. 7892–7895. DOI: 10.1103/PhysRevB.41.7892.

[28] C. C. Marston and G. G. Balint-Kurti. "The Fourier Grid Hamiltonian Method for Bound State Eigenvalues and Eigenfunctions". In: *J. Chem. Phys.* 91 (1989), pp. 3571–3576. DOI: 10.1063/1.456888.

[29] F. R. Kroeger and C. A. Swenson. "Absolute Linear Thermal-Expansion Measurements on Copper and Aluminum from 5 to 320 K". In: *J. Appl. Phys.* 48 (1977), pp. 853–864. DOI: 10.1063/1.323746.

[30] K. H. Chae, H. C. Lu, and T. Gustafsson. "Medium-Energy Ion-Scattering Study of the Temperature Dependence of the Structure of Cu(111)". In: *Phys. Rev. B* 54 (1996), pp. 14082–14086. DOI: 10.1103/PhysRevB.54.14082.

[31] V. F. Sears and S. A. Shelley. "DebyeFactor for Elemental Crystals". In: *Acta. Cryst. A* 47 (1991), pp. 441–446. DOI: 10.1107/S0108767391002970.

[32] J. Stoer and R. Bulirsch. *Introduction to Numerical Analysis*. New York: Springer-Verlag, 1980.

[33] S. Nave and B. Jackson. "Methane Dissociation on Ni(111): The Effects of Lattice Motion and Relaxation on Reactivity". In: *J. Chem. Phys.* 127 (2007), p. 224702. DOI: 10.1063/1.2800661.

[34] F. Battaglia and F. A. Gianturco. "Vibrational Relaxation of HF Colliding with Helium. A Coupled Quantum Treatment". In: *Chem. Phys.* 55 (1981), pp. 283–291. DOI: 10.1016/0301-0104(81)80264-9.

[35] M. C. van Hemert. "Potential Energy Surface for the Study of Inelastic Collisions between Nonrigid CO and H2". In: *J. Chem. Phys.* 78 (1983), pp. 2345–2354. DOI: 10.1063/1.445034.

[36] Y. Xiao, W. Dong, and H. F. Busnengo. "Reactive Force Fields for Surface Chemical Reactions: A Case Study with Hydrogen Dissociation on Pd Surfaces". In: *J. Chem. Phys.* 132 (2010), p. 014704. DOI: 10.1063/1.3265854.

[37] F. Nattino, C. Díaz, B. Jackson, and G.-J. Kroes. "Effect of Surface Motion on the Rotational Quadrupole Alignment Parameter of D_2 Reacting on Cu(111)". In: *Phys. Rev. Lett.* 108 (2012), p. 236104. DOI: 10.1103/PhysRevLett.108.236104.

[38] M. Wijzenbroek and G.-J. Kroes. "The Effect of the Exchange-Correlation Functional on H2 Dissociation on Ru(0001)". In: *J. Chem. Phys.* 140 (2014), p. 084702. DOI: 10.1063/1.4865946.

[39] R. D. Muino and H. F. Busnengo. *Dynamics of Gas-Surface Interactions: Atomic-Level Understanding of Scattering Processes at Surfaces*. Springer Series in Surface Sciences. Berlin Heidelberg: Springer-Verlag, 2013.

[40] M. Bonfanti, C. Díaz, M. F. Somers, and G.-J. Kroes. "Hydrogen Dissociation on Cu(111): The Influence of Lattice Motion. Part I". In: *Phys. Chem. Chem. Phys.* 13 (2011), pp. 4552–4561. DOI: 10.1039/C0CP01746A.

[41] S. Kaufmann, Q. Shuai, D. J. Auerbach, D. Schwarzer, and A. M. Wodtke. "Associative Desorption of Hydrogen Isotopologues from Copper Surfaces: Characterization of Two Reaction Mechanisms". In: *J. Chem. Phys.* 148 (2018), p. 194703. DOI: 10.1063/1.5025666.

[42] S. M. Foiles, M. I. Baskes, and M. S. Daw. "Embedded-Atom-Method Functions for the Fcc Metals Cu, Ag, Au, Ni, Pd, Pt, and Their Alloys". In: *Phys. Rev. B* 33 (1986), pp. 7983–7991. DOI: 10.1103/PhysRevB.33.7983.

[43] Y. Mishin, M. J. Mehl, D. A. Papaconstantopoulos, A. F. Voter, and J. D. Kress. "Structural Stability and Lattice Defects in Copper: Ab Initio, Tight-Binding, and Embedded-Atom Calculations". In: *Phys. Rev. B* 63 (2001), p. 224106. DOI: 10.1103/PhysRevB.63.224106.

[44] B.-J. Lee, J.-H. Shim, and M. I. Baskes. “Semiempirical Atomic Potentials for the Fcc Metals Cu, Ag, Au, Ni, Pd, Pt, Al, and Pb Based on First and Second Nearest-Neighbor Modified Embedded Atom Method”. In: *Phys. Rev. B* 68 (2003), p. 144112. DOI: 10.1103/PhysRevB.68.144112.

[45] H. W. Sheng, M. J. Kramer, A. Cadien, T. Fujita, and M. W. Chen. “Highly Optimized Embedded-Atom-Method Potentials for Fourteen Fcc Metals”. In: *Phys. Rev. B* 83 (2011), p. 134118. DOI: 10.1103/PhysRevB.83.134118.